Neurobiology of Disease 124 (2019) 340–352

Contents lists available at ScienceDirect

Neurobiology of Disease

journal homepage: www.elsevier.com/locate/ynbdi

Muscle specific kinase (MuSK) activation preserves neuromuscular junctions in the diaphragm but is not sufficient to provide a functional benefit in the SOD1^{G93A} mouse model of ALS

Arundhati Sengupta-Ghosh[a,1], Sara L. Dominguez[a,1], Luke Xie[b], Kai H. Barck[b], Zhiyu Jiang[a], Timothy Earr[a], Jose Imperio[a], Lilian Phu[c], Hanna G. Budayeva[c], Donald S. Kirkpatrick[c], Hao Cai[e], Jeffrey Eastham-Anderson[d], Hai Ngu[d], Oded Foreman[d], Maj Hedehus[b], Michael Reichelt[d], Isidro Hotzel[f], Yonglei Shang[f], Richard A.D. Carano[b], Gai Ayalon[a], Amy Easton[a,*]

[a] Departments of Neuroscience, Genentech, South San Francisco, CA, USA
[b] Departments of Biomedical Imaging, Genentech, South San Francisco, CA, USA
[c] Departments of Microchemistry, Proteomics, and Lipidomics, Genentech, South San Francisco, CA, USA
[d] Departments of Pathology, Genentech, South San Francisco, CA, USA
[e] Departments of Preclinical and Translational Pharmacokinetics, Genentech, South San Francisco, CA, USA
[f] Departments of Antibody Discovery, Genentech, South San Francisco, CA, USA

ARTICLE INFO

Keywords:
SOD1
Amyotrophic lateral sclerosis
Muscle specific kinase (MuSK)
Respiration
Diaphragm
Neuromuscular junction
Motor Neuron

ABSTRACT

Amyotrophic lateral sclerosis (ALS), a neurodegenerative disease affecting motor neurons, is characterized by rapid decline of motor function and ultimately respiratory failure. As motor neuron death occurs late in the disease, therapeutics that prevent the initial disassembly of the neuromuscular junction may offer optimal functional benefit and delay disease progression. To test this hypothesis, we treated the SOD1^{G93A} mouse model of ALS with an agonist antibody to muscle specific kinase (MuSK), a receptor tyrosine kinase required for the formation and maintenance of the neuromuscular junction. Chronic MuSK antibody treatment fully preserved innervation of the neuromuscular junction when compared with control-treated mice; however, no preservation of diaphragm function, motor neurons, or survival benefit was detected. These data show that anatomical preservation of neuromuscular junctions in the diaphragm via MuSK activation does not correlate with functional benefit in SOD1^{G93A} mice, suggesting caution in employing MuSK activation as a therapeutic strategy for ALS patients.

1. Introduction

Degeneration of motor neurons leads to motor symptoms and rapid functional decline in patients diagnosed with amyotrophic lateral sclerosis (ALS). Pathology is detected throughout all regions of the motor neuron from the cell body in the CNS to peripheral axons, axon terminals, as well as in the muscle. Synapse loss at the neuromuscular junction (NMJ) is a key pathological event, detectable at the onset of motor symptoms, and in some cases prior to motor neuron loss (Fischer et al., 2004). To date, treatments aimed at preservation of the motor neuron cell body have resulted in modest delay of disease progression and survival benefit (Kostic et al., 1997; Fischer et al., 2004). Therapeutic interventions that preserve neuromuscular synapses may present an opportunity to slow the loss of motor function, improving quality of life for patients. If denervation of the NMJ precipitates motor neuron loss, such therapeutic interventions may also delay the death of motor neurons and extend survival.

Muscle specific kinase (MuSK) is expressed on the post-synaptic membrane at the neuromuscular junction where it associates with low-density lipoprotein receptor-related protein 4 (LRP4) to regulate proper development and function of mature NMJs (DeChiara et al., 1996). Agrin, a proteoglycan secreted from the motor neuron, binds to the MuSK-LRP4 complex, leading to phosphorylation and stabilization of acetylcholine receptors on the muscle (Burden et al., 2013). The MuSK-LRP4 complex also signals back to motor axons to stimulate their attachment and differentiation (Yumoto et al., 2012). MuSK function-

* Corresponding author at: 1 DNA Way, South San Francisco, CA 94080, United States.
E-mail address: easton.amy@gene.com (A. Easton).
[1] These authors contributed equally.

https://doi.org/10.1016/j.nbd.2018.12.002
Received 3 August 2018; Received in revised form 12 November 2018; Accepted 3 December 2018
Available online 04 December 2018
0969-9961/

blocking antibodies can cause shrinkage of nerve terminals at NMJs, misalignment of the pre- and post-synaptic membranes and muscle weakness in rodents (Cole et al., 2008; Morsch et al., 2012) and can lead to NMJ disorders such as myasethenia gravis (Engel et al., 2015).

While there is no known genetic association of MuSK with ALS risk or progression, previous studies on MuSK signaling suggest that activating MuSK may be beneficial. Indeed, overexpression of MuSK has been shown to temporarily prevent muscle denervation and delay motor dysfunction in the SOD1^{G93A} mouse (Perez-Garcia and Burden, 2012). In addition, a recent study showed that an activating MuSK antibody prevented NMJ loss in the diaphragm, protecting motor neurons and improving motor function in an ex vivo assay of muscle fatigue (Cantor et al., 2018). We therefore investigated whether chronic treatment with an activating MuSK antibody affects innervation and function of the diaphragm, motor neuron protection, and survival in SOD1^{G93A} mice. We used a combination of techniques to measure diaphragm function including direct measure of the diaphragm compound muscle action potential, measurement of respiration via micro-CT imaging of the lung, and whole-body plethysmography. We found that anti-MuSK treatment resulted in robust preservation of the neuromuscular junction in the diaphragm but yielded no functional benefit.

2. Methods

2.1. SOD1^{G93A} mouse model of ALS

SOD1^{G93A} high copy number transgenic mice and their non-transgenic littermates were originally derived from Jackson Laboratory (Bar Harbor, ME; stock #002726) (Gurney et al., 1994) and were back-crossed at Genentech for > 20 generations into C57BL/6 N (Charles River). Mice were housed on a regular light/dark cycle (14:10 h) with ad libitum access to food (LabDiet 5010) and water. All behavioral assessments were conducted during the light phase. For copy number calculations DNA concentration of both experimental and SOD1 control samples were normalized to 30 ng/μl. Control DNA was isolated from tail biopsies provided by The Jackson Laboratory (strain #002726), which had been previously reported as approximately 30 copies/genome (Livak and Schmittgen, 2001). Routine copy number variation was performed as previously described (Alexander et al., 2004). Methods and amplification conditions are provided in the Supplementary Materials. All animals enrolled into the study fell into the expected high copy number range as described above.

2.2. Anti-MuSK antibody

MuSK activating antibody (MuSK #13) was derived from human naïve phage library as previously described (Xie et al., 1997). The antibody light and heavy chain variable regions (see supplementary materials) were obtained by gene synthesis (Genewiz) and subcloned into mammalian expression vectors with the mouse Kappa and mouse IgG2a LALAPG (L234A, L235A and P329P mutations, Eu index) constant regions, respectively, creating a human variable/mouse constant chimeric antibody. The antibody transiently expressed in Chinese hamster ovary cells and affinity purified with protein A chromatography followed by size exclusion with a Superdex200 column.

2.3. LC-MS

C2C12 mouse myoblasts were differentiated for 10 days and then activated with Agrin or MuSK antibody for indicated time periods. Cells were quickly rinsed with cold PBS and harvested in 50 mM Tris, 0.15 M NaCl,1 mM EDTA containing protease and phosphatase inhibitors (Roche). Immunoprecipitation (IP) was performed using rabbit anti-MuSK antibody (kindly provided by Stephen Burden) and sepharose A magnetic beads (GE). Bound protein mixture was eluted with SDS loading buffer containing reducing agent by boiling samples. IP samples were separated on SDS-PAGE. Gel regions of interest (around 100 kDa) were excised, reduced and alkylated before in-gel digestion with trypsin. Digested peptide mixture was analyzed by LC-MS/MS on Waters nanoAcquity UPLC coupled to Thermo Orbitrap-Elite mass spectrometer. Peptides were directly loaded onto a 100um X 100 mm 1.7um BEH C18 column (Waters) and separated with a 45-min linear gradient where buffer B (2% acetonitrile, 0.1%FA) was ramped from 2% to 25%. Orbitrap-Elite was set to data-dependent acquisition mode with full MS scan at 60,000 resolution, followed by collision-induced dissociation and MS/MS on the top 15 most abundant ions from the MS scan. MS/MS spectra were searched using Mascot software against mouse UniProt sequence database (downloaded April 2015) with the following settings: precursor mass tolerance at 50 ppm, fixed modification: carbamidomethylation on Cys; variable modifications: oxidation on Met, phosphorylation on Set, Thr, Tyr. Data were filtered to 1% FDR using linear discriminant analysis. Ascore algorithm was used for phosphorylation site assignment. Extracted ion chromatograms were obtained over +/− 5 ppm window using XCalibur software (Thermo Fisher Scientific).

2.4. Drug formulation

MuSK antibody was freshly formulated on the day of dosing by diluting in sterile saline to 10 mg/ml for 100 mg/kg dose level or 1 mg/ml for the 10 mg/kg dose level.

Anti-gp120 antibody was also formulated in sterile saline 10 mg/ml and was used as the control.

2.5. Study design

The study design included two cohorts of animals - one cohort for MRI and functional assessment and a second cohort used for histological assessment of NMJs and motor neuron loss. Mice were assigned to treatment groups at 4 weeks of age. SOD1.tg mice were pseudorandomized to one of three treatment groups, balanced for sex and litter. Treatments included 100 mg/kg anti-gp120 and 10 or 100 mg/kg MuSK #13 with equal males and females entered into each treatment group (n = 10–12/sex/treatment). The same treatment groups were included for the histology cohort (n = 5/sex/treatment), given the same dosing solution as the functional cohort. Based on the simulated concentration in muscle tissue, a 10 mg/kg dose was selected to guarantee a steady state muscle concentration of MuSK #13 higher than the in vitro EC_{90} (Herbst and Burden, 2000). A high dose of 100 mg/kg was also included in this study to provide a 10-fold margin over the EC_{90} with consideration of individual variation and the accuracy of extrapolating in vitro EC_{90} to in vivo. SOD1.tg mice were compared to wild-type, littermates treated with the control antibody anti-gp120. Antibody was given via intraperitoneal (i.p.) injections once every two weeks starting at 6 weeks of age, prior to disease onset. Dosing continued out to 18 weeks of age for the histology cohort and to 22 weeks of age for the functional cohort. Mice were weighed the day before dosing so that dose volumes would accurately reflect changes in weight. All functional assessments were conducted prior to disease onset and at multiple time points throughout the time course of the disease in mice (Fig. 2.)

The animals were housed by treatment group. At 15 weeks of age all cages received soft food (DietGel® 76A, PharmaServ) 1 × weekly and at 18 weeks of age diet gel was replaced daily, such that all mice equally received supplements well before the onset of paralysis symptoms. Most importantly, all mice, regardless of paralysis level were able to reach food/water. All protocols for mouse experiments were approved by the Institutional Animal Care and Use Committee and were conducted in accordance with the NIH Guide for the Care and Use of Laboratory Animals.

2.6. Blood sampling and plasma separation

To measure peripheral exposure levels of our antibodies in the mice, blood was collected via retro-orbital bleeding. Up to 100 µl of blood was collected and mice were given 100 µl of replacement fluids to assist in recovery and monitored following the bleeds. Blood was collected in K2 EDTA Micro500 tubes (part# M500-E, SAI Infusion Technologies), stored on ice until all samples were collected and then spun down at 4 °C for 3 min at maximum speed. The plasma was pipetted into clean tubes and immediately frozen at -80 °C until processed.

2.7. Measurement of antibody levels in plasma

In vivo plasma concentration of MuSK #13 mouse IgG2a was measured by ELISA. NUNC (Neptune, NJ) 384-well maxisorp immunoplates were coated with mouse anti-mouse IgG2a (allotype A specific) antibody (Pharmingen) in PBS overnight at 4 °C. The following day, plates were washed 3 times with PBS/0.05% Tween 20 and blocked in PBS/0.5% BSA/15PPM ProClin, pH 7.4 for 1 h at room temperature on an orbital shaker. MuSK antibody standards (1.56–100 ng/ml) and mouse serum samples were all prepared in assay buffer (PBS/0.5% BSA/0.35 M NaCl/0.25% CHAPS/5 mM EDTA/0.2% bovine gamma globulin/0.05% Tween 20/15PPM ProClin, pH 7.4) were added to plates and incubated at room temperature for 2 h with shaking. Rat anti-mouse IgG2a conjugated to horseradish peroxidase (GeneTex, Inc) was prepared in PBS/0.5%BSA/0.05% Tween20/15PPM proClin, pH 7.4, added to plates and incubated at room temperature for 30 min. Finally, plates were developed using the substrate 3,3′,5,5′-tetramethyl benzidine (TMB) (KPL, Inc., Gaithersburg, MD). Absorbance was measured at a wavelength of 450 nm with a reference of 630 nm on a Multiskan Ascent reader (Thermo Scientific, Hudson, NH). Concentrations were determined from the standard curve using a four-parameter non-linear regression program using software developed at Genentech. This assay has a minimum required dilution of 1:100 and a low limit of quantification of 156 ng/ml in serum. Simulated plasma concentrations of antibody in multi-dose treatment of MuSK #13 were obtained using a two-compartment pharmacokinetic (PK) model, which was established by fitting the model to the reported data from single dose mouse PK study (Herbst and Burden, 2000). Concentrations of antibody in muscle tissues were estimated by applying a tissue: plasma partition coefficient to the simulated plasma concentrations. Partition coefficient was obtained from published results (Yip et al., 2014; Li et al., 2016). All PK parameter calculations and simulations were performed using WinNolin 6.4 (Pharsight, Mountain View, CA).

2.8. Tissue harvest and preparation

Mice were euthanized using 2.5% tribromoethanol (0.5 ml/25 g body weight) and transcardially exsanguinated with phosphate-buffered saline (PBS), followed by 4% pararformaldehyde (PFA) in PBS for fixation. Diaphragm muscles were harvested prior to PFA perfusion. Diaphragms were then stretched using pins on sylguard plates and fixed using 2% PFA for 2 h, this allowed better penetration of antibodies in the whole mount preparation. Spinal cords were dissected and post-fixed overnight in 4% PFA, then transferred into PBS and shipped to NeuroScience Associates (Knoxville, TN) for histology.

2.9. Immunohistochemistry (IHC) for motor neurons and NMJs

Lumbar and cervical spinal cords were sectioned and stained as described in Le Pichon et al., 2013. Tissues were multiple-embedded into a gelatin matrix using MultiBrain Technology (NeuroScience Associates) and each MultiBrain block was sectioned coronally at 25 µm. A series of 33 sections, equally spaced at 300 mm intervals throughout either the entire lumbar or cervical spinal cord was used for staining. IHC staining was performed using goat anti-ChAT (choline acetyltransferase; Millipore AB144P) at 1:1000. Whole slide imaging was performed at 200× magnification using the Nanozoomer (Hamamatsu Corp, San Jose, CA) system. Images were analyzed using Matlab (Mathworks, Natick, MA). Tissue sections and motor neurons were detected using color thresholds and morphological operations. A regional minima and radial symmetry detection (Veta et al., 2013) with watershed segmentation followed by morphological, shape and size filtering was used to further enumerate DAB positive motor neurons. Image analysis was performed by a scientist blinded to experimental grouping and genotype.

NMJ analysis was conducted on the diaphragm, the muscle most relevant to primary functional measures of respiration. The unique structure of the diaphragm muscle tissue enables histology in a whole mount preparation without sectioning. Innervation and denervation of the NMJs can be quantified in the entire tissue for each animal. Diaphragms were harvested from 18-week-old SOD1.tg mice, post PBS perfusion. Alexa 488-conjugated alpha bungarotoxin (Life Technologies) was used to label post synaptic terminal (AChRs) and rabbit Neurofilament-L (SYnaptic Systems), rabbit Synapsin 1/2 (SYnaptic Systems) was used to label axons and presynaptic nerve terminals. Alexa-594 donkey anti-rabbit antibody was used as secondary antibody (Life Technologies). Diaphragms were whole mounted on slides using Flouromount-G and Z stack images were captured using a confocal microscope. Images were analyzed in the Matlab software package (version R2017a by Mathworks, Natick, MA). Individual NMJs events were identified using standard intensity thresholding and morphologic processing in the α − bungarotoxin channel. The number of pixels that had an overlap with the presynaptic staining channel was then quantified for each NMJ (Van de Lest et al., 1995). Approximately 150 NMJs per animal were quantified. NMJs with 0–5% co-localization of staining were marked as denervated, 100–75% pixel co-localization were marked as innervated while 75% to 5% co-localization was marked as partially innervated.

2.10. Compound muscle action potential (CMAP) measurement in diaphragm

CMAP amplitudes were assessed at 11, 16, and 19 weeks of age. Mice were anesthetized with 2.5% isoflurane, chest and neck areas were shaved and remaining hair was removed. Two stimulating needle electrodes were inserted transcutaneously into the phrenic nerve on the right side of the neck, lateral to the trachea and superior to the clavicle. A self-adhesive surface recording electrode was placed transversely along the right of the unilateral costal margin. A reference needle electrode was inserted into the contralateral lower abdominal region and a digital ring ground electrode, coated in electrode cream, was placed on the mouse's tail. Data was amplified (BioAmp, ADinstruments) and acquired with a sampling rate of 10 kHz and a 0.3 Hz single stimulation frequency (Powerlab 4/25, ADInstruments). A controlled stimulus with a pulse duration of 0.5 ms was applied to the nerve to evoke contractions from the diaphragm. The optimal current to achieve a maximal response was determined by increasing the current from 2 mA to as high as 50 mA until the amplitude no longer increased. After the maximum response was found, an average of each mouse's maximum amplitude was collected by sampling 10 repeats from the optimal, fixed current with 10 s intervals between each stimulus.

2.11. Micro-computed tomography (micro-CT)

Micro-CT imaging with retrospective respiratory gating was performed to measure respiratory dynamics in the mice at 9, 17, and 21 weeks of age. Images were acquired on an in vivo micro-CT scanner (U-CT^{UHR}, MILabs, Utrecht, The Netherlands), with the following settings: gated total-body scan mode, 65 kV voltage, 0.13 mA current, 20 ms exposure, 2 × 2 binning, 1° angle step, and 16 projections/angle.

The acquisition time was 5 min. Anesthesia was induced and maintained throughout the imaging with 3.75% sevoflurane in 1 LPM air. During the imaging, the animals were kept warm with a heating pad and their respiration was monitored by a BioVet system (m2 m Imaging, Cleveland, OH, USA), with trigger points being recorded at the start of inspiration. Images of the thoracic region were reconstructed for peak inspiration and end-expiration phases of the respiration cycle at 80 μm isotropic voxel size and filtered with 200 μm Gaussian smooth filter. In-house image analysis software was written in C++ using Analyze AVW image processing functions (AnalyzeDirect Inc., Lenexa, KS, USA) to automatically segment the lung air space, including the alveolar tissue and airways. The air space was segmented by intensity thresholding (< -200 HU) and finding the largest connected object within the mouse body. The anterior boundary of the segmented region within the trachea was set to 2.4 mm distal from the tracheal bifurcation. The algorithm to find the tracheal bifurcation has been previously described in detail (Barck et al., 2015). Tidal volume was defined as the lung volume difference between peak inspiration and end-expiration images. At the 21-week imaging time point, a hypercapnia challenge was applied after the regular (air condition) micro-CT acquisition. The anesthesia carrier gas was switched from air to a mixture of 5% CO_2, 21% O_2, 74% N_2. The animal was then allowed to stabilize for 5 min, followed by a micro-CT acquisition under the hypercapnia condition. Tidal Volume for both the air and hypercapnia states and change in Tidal Volume from air to hypercapnia state (Delta Tidal Volume) were calculated for each mouse at the 21-week time point.

2.12. Whole-body plethysmography

Respiratory function was assessed in awake, unrestrained mice using a FinePointe Whole-Body Plethysmography 4 site system (DSI, St. Paul, MN). Mice were put into individual plethysmography chambers and acclimated for 30 min before a 30 min recording session. Calibrated chamber pressure, temperature and humidity were collected by a transducer and signals were amplified, digitized, and analyzed by the packaged FinePointe software. Tidal volume, minute volume, and breathing frequency were calculated from differences in air pressure between the test and reference chamber. Respiration was recorded at ages 8, 18, 20, 21 and 22 weeks. For each animal, an average across the 30 min was calculated and used to generate the group mean for each time point. On week 20, after the routine 30 min acclimation and 30 min recording session, the chamber air was replaced with 5% CO2 mixed with regular air for 30 min and then switched back to room air for 15 min.

2.13. MRI imaging

MRI was performed on a Bruker 7 T (Billerica, MA) with a volume transmit and cryogenic surface receive coil. A custom in vivo holder was constructed with 3D printing (Stratasys Dimension) to provide secure positioning of the brain and spine. A T_2 map covering hindbrain and cervical spinal cord was generated with a multi-slice multi-echo sequence with these parameters: TR = 4 s, TE_1/spacing/TE_8 = 10/10/80 ms (8 echoes), BW = 50 kHz, matrix = 160 × 160 × 40, resolution = 125 × 125 × 400 μm^3. Two DTI scans (single-shot EPI) with individual local shims were used for the hindbrain and spinal cord with these parameters: TR = 4 s, TE = 42 ms, BW = 250 kHz, gradient directions = 20, encoding matrix = 104 × 102 × 20, reconstructed matrix = 128 × 128 × 20, reconstructed resolution = 141 × 141 × 400 μm^3. Datasets were used to compute T_2 and DTI parametric maps: fractional anisotropy (FA), mean diffusivity (MD), axial diffusivity (AD), and radial diffusivity (RD). Data were analyzed in the hindbrain (hypoglossal nucleus, nucleus ambiguous, facial nucleus, and trigeminal nucleus) and in the ventral side of cervical spinal cord (approximately C1 to C5 vertebrae).

2.14. Body weight

Weights were recorded every other week until 16 weeks of age and then weekly. Once a mouse was within one gram of its takedown weight (measured as a 20% drop from their adult body weight) that mouse was weighed daily until takedown criteria were met. Adult body weight was defined as the weight at 12 weeks of age.

2.15. Paralysis scoring

Paralysis scoring using the ALS TDI neurological scores of 2–4 (Hatzipetros, 2015) began at 112 days, well before the onset of these particular paralysis symptoms. The scoring used here differed only in that score of 4 had a 15 s righting time limit instead of 10 s in the traditional scoring system. Scoring was recorded separately for each hind paw. The day that the mouse progressed to the next score and repeated that score at the following measure was reported as its age of onset for that particular score.

2.16. Criteria for euthanasia (survival)

Once mice reached a paralysis score of 4 they were euthanized. The criteria included: 1) the inability of the mouse to right itself within 15 s and/or 2) a 20% decrease in body weight from that mouse's adult body weight, taken at 12 weeks of age.

2.17. Statistics

Statistical analyses were performed using Graphpad Prism v7.0 and MRI data analysis was conducted in MATLAB (Mathworks, Natick, MA). Unless otherwise indicated, a RM ANOVA was conducted on the time course data presented followed by a Dunnett's post-hoc analysis. For bar graphs, a t-test was used to test for a genotype effect. A one-way ANOVA followed by Dunnett's post-hoc was used test for treatment effects between the vehicle and MuSK #13 treatment groups.

3. Results

3.1. MuSK #13 activates MuSK in vitro

We first determined whether MuSK #13 could activate its target in vitro. The effect of antibody treatment on MuSK activation was tested in a series of experiments determining MuSK phosphorylation status in C2C12 myotubes. It was previously reported that MuSK phosphorylation at Tyr553 (pY553) is required for downstream signal propagation upon agrin stimulation (Herbst and Burden, 2000). To assess MuSK phosphorylation, endogenous MuSK was isolated by immunoaffinity purification (IP) from differentiated C2C12 mouse myoblasts treated with agrin or MuSK #13 for 30 or 60 min. As controls, IPs were performed from lysates of HEK293, and differentiated but untreated C2C12. Increased levels of total phospho-Tyr, as well as phospho-MuSK were detected in agrin- and MuSK #13-treated cells, as compared to controls (Fig. 1A). Phosphorylation was not detected in IPs from HEK293 or undifferentiated C2C12 cells. Total MuSK was present at negligible levels in undifferentiated C2C12 cells and below the limit of detection in HEK293 cells, as expected. Next, MuSK phosphorylation status was determined by mass spectrometry analysis of IP samples (Fig. 1B and C). MuSK IP was resolved by gel electrophoresis, stained with Coomassie, and gel bands excised from a region corresponding to the expected molecular weight for MuSK. Digested peptides were extracted and analyzed by liquid chromatography-tandem MS (LC-MS/MS). MuSK pY553 peptide was identified by MS/MS with high confidence (Fig. 1B). The peptide indicative of pY553 from MuSK displayed higher relative abundance in IPs from agrin- and MuSK #13-treated samples compared to IPs from the untreated C2C12 (Fig. 1C, left panel). As a comparison, total MuSK levels measured by unmodified MuSK

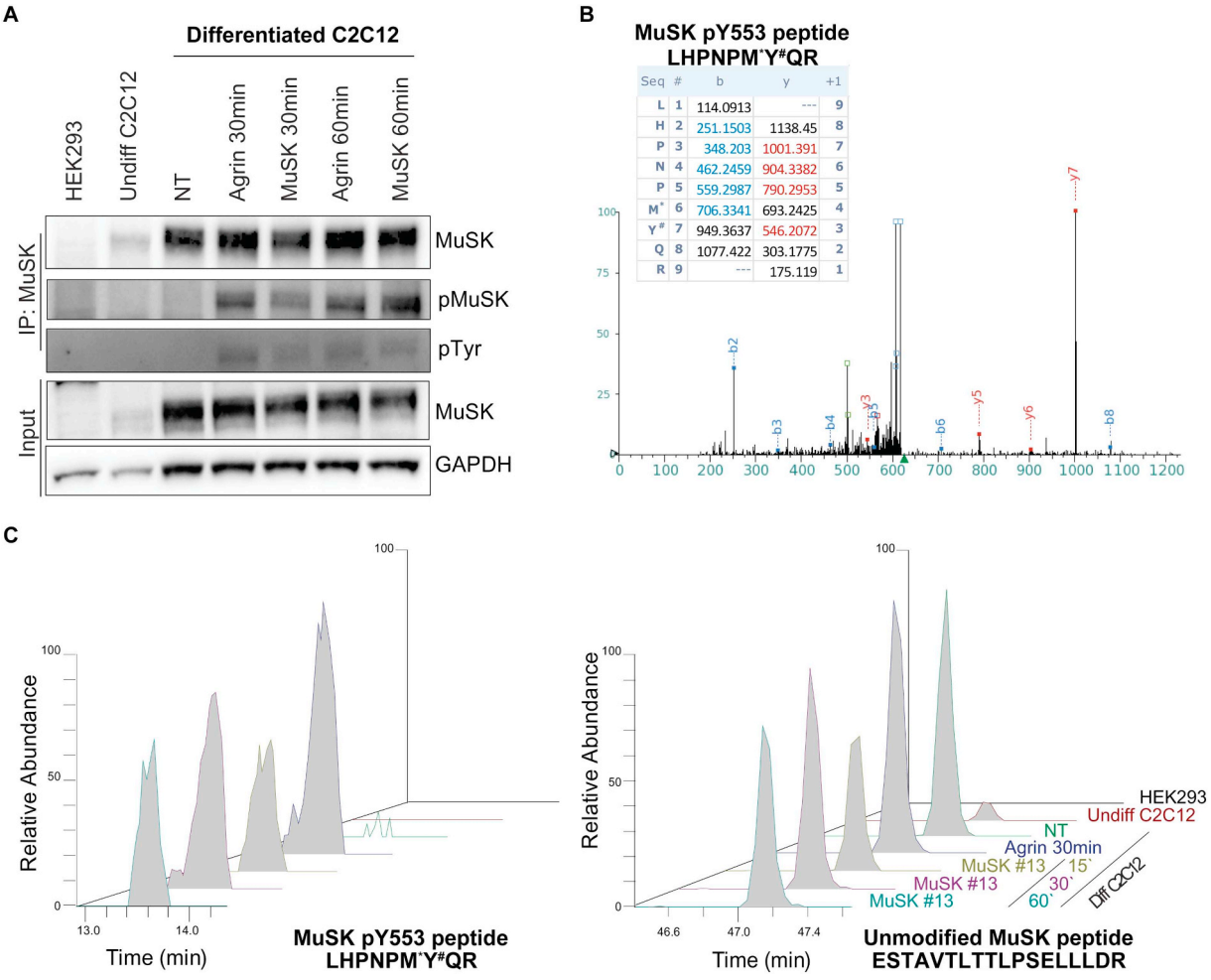

Fig. 1. Induction of MuSK phosphorylation at Y553 upon activation with agrin or MuSK antibody. A. Immunoprecipitation (IP) and Western Blot of endogenous MuSK from untreated HEK293, undifferentiated C2C12, and differentiated C2C12 cells. Differentiated C2C12 cells were either untreated (NT), treated with agrin, or treated with the MuSK-activating antibody at the indicated time points. IP eluates were probed with antibodies recognizing MuSK, phosphorylated MuSK or phosphorylated Tyr, while IP input samples were probed with total MuSK and GAPDH as loading controls. B. MS/MS spectrum of peptide demonstrating identification of MuSK phosphorylation site at Y553 ($Y^{\#}$). The presence of oxidized methionine (M^{*}) is also noted. C. Extracted ion chromatograms demonstrating the relative abundance of MuSK pY553 (LHPNPM*Y#QR; z = 2, 626.2708 *m/z*) and an unmodified MuSK peptide (ESTAVTLTTLPSELLLDR; z = 2, 980.0373 m/z) in endogenous MuSK IP from indicated samples.

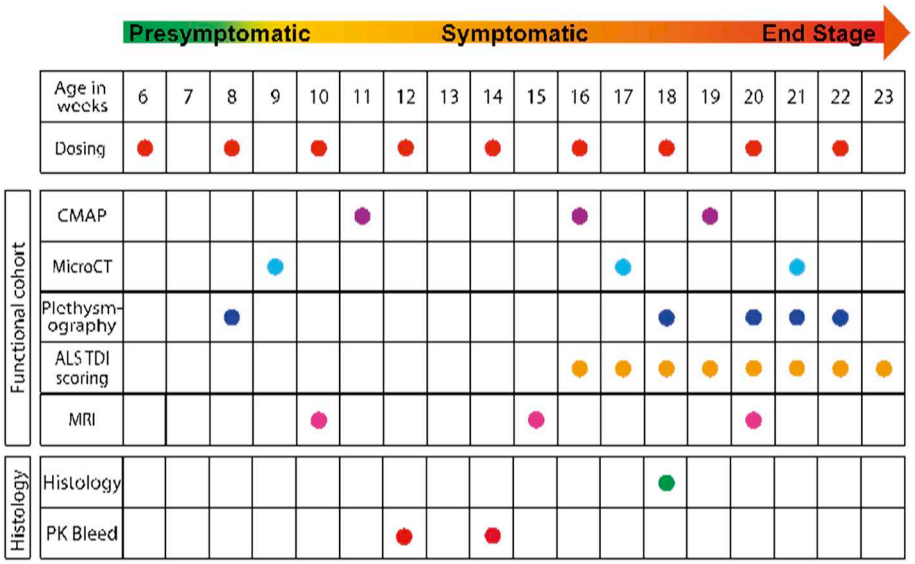

Fig. 2. Study design. Schematic representation of functional and histological assessment with respect to dosing and symptoms. Dosing (10 or 100 mg/kg, i.p.) for functional and histology cohorts occurred once every 2 weeks as indicated by red dots. Each functional assessment, represented by a different color dot, was conducted on at least 3 occasions throughout the course of the disease. NMJ and motor neuron analysis was conducted at 18 weeks only as indicated by the green dot. Blood was collected for MuSK concentrations at the projected C_{min} and C_{max} halfway through the study. (For interpretation of the references to color in this figure legend, the reader is referred to the web version of this article.)

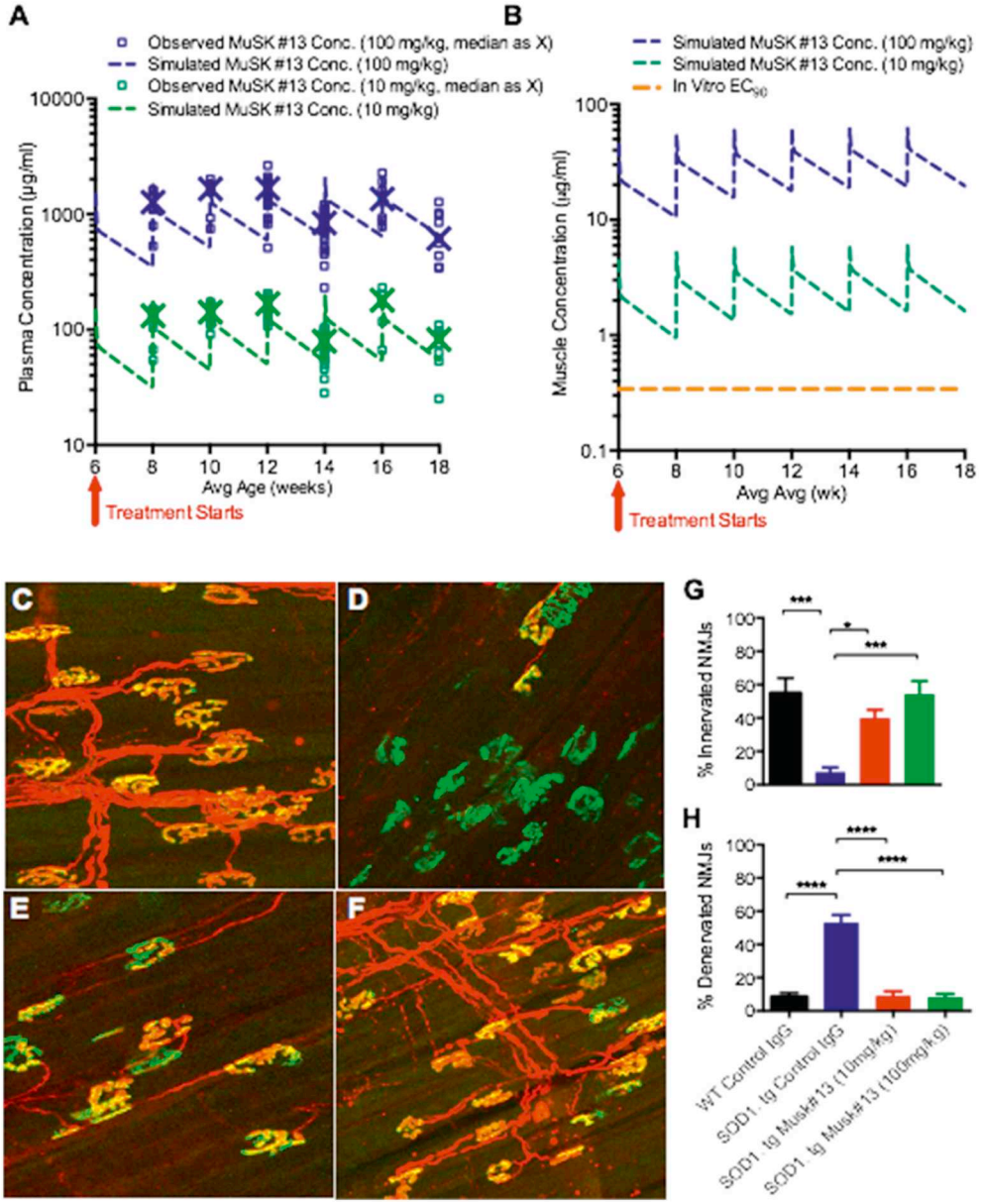

Fig. 3. Anti-MuSK PK, target engagement and NMJ protection in SOD1 diaphragm. A. The observed individual (square) and median (cross) plasma concentrations of MuSK #13 were overlaid with simulated concentrations based on PK model (dash line) at 10 mg/kg and 100 mg/kg doses. B. Concentrations of MuSK #13 in muscle tissues were simulated and compared with EC_{90} from in vitro study. C. WT, Control IgG group D. SOD1.tg, Control IgG E. SOD1.tg, MuSK #13 (10 mg/kg) F. SOD1.tg, MuSK #13 (100 mg/kg)(C–H). Dosing SOD1.tg mice with MuSK #13 for 13 weeks protects against NMJ denervation. Maximum projection images of wholemount diaphragm stained with alpha bungarotoxin (green) and rabbit anti-Neurofilament light and rabbit anti-Synapsin (red). (G-H) SOD1 tg animals dosed with GP120 had a greatly diminished number of innervated NMJs remaining compared to the WT (***P = .0005), while SOD1.tg dosed with MuSK agonist antibody have significantly more innervated NMJs (SOD1. tg control vs SOD1 MuSK 10 mg/kg, *P = .023) (SOD1 tg control vs SOD1 MuSK 100 mg/kg, ***P = .0006). Similarly, SOD1.tg animals dosed with GP120 had mostly completely denervated NMJs (****P < .0001) when compared to WT, while SOD1 tg dosed with MuSK agonist antibody had reduced number of completely denervated NMJs (****P < .0001). NMJ data plotted as mean ± SEM (n = 6–7 animals per group).

peptide were not significantly different in IPs from untreated and treated samples (Fig. 1C, right panel). Overall, these results confirm that the MuSK #13 antibody functions as a potent MuSK activator in cultured myotubes and are consistent with published data demonstrating MuSK activity with this antibody in C2C12 cells (Xie et al., 1997).

3.2. MuSK #13 protects neuromuscular junctions (NMJs) against denervation

MuSK #13 was engineered to have a murine back-bone that allows chronic dosing in mice with relatively low clearance. This agonist antibody was shown to localize to neuromuscular junctions in mice given a 10 mg/kg dose of antibody (Cantor et al., 2018). MuSK #13 exhibited an expected PK profile as the observed plasma concentrations of MuSK #13 were dose-proportional at the two dose levels and aligned well with the simulated plasma concentrations (Fig. 3A). Although the concentrations of MuSK #13 in muscle tissues were not measured, simulation showed that steady state trough antibody concentrations in muscle tissues at 10 and 100 mg/kg doses were 5-fold and 50-fold higher than in vitro EC_{90} (Fig. 3B), suggesting both dose levels could achieve sufficient target engagement in muscles.

Since we intended to focus on diaphragm function, we chose to measure innervation of the NMJ in the diaphragm at 18 weeks of age. At this time point, maximal degeneration of motor neurons was observed in the cervical spinal cord (supplemental fig. 1A). To determine whether chronic MuSK #13 treatment could retain NMJ connectivity in vivo, we conducted whole mount IHC on the diaphragm of wild-type and SOD1.tg mice treated with MuSK #13 or control antibody. SOD1.tg mice showed a robust loss of NMJ innervation compared to wild-type littermates, as expected from a previous time course study. Wild-type mice had 54.88% ± 9.07% completely innervated and 7.9% ± 3.3% completely denervated NMJs, while SOD1.tg mice had 7.06% ± 2.73% completely innervated and 50.38% ± 6.77% completely denervated NMJs (Fig. 3C-D, G-H). MuSK #13 antibody treatment resulted in an increase in innervated NMJs and a decrease in denervated NMJs at both 10 mg/kg and 100 mg/kg dose levels (Fig. 3E-F). The proportion of innervated NMJs in 10 mg/kg increased to 39.92% ± 4.99% and 54.36% ± 7.84% in 100 mg/kg, while the proportion of denervated NMJs reduced to 9.04% ± 2.72% in the 10 mg/kg dosed group and

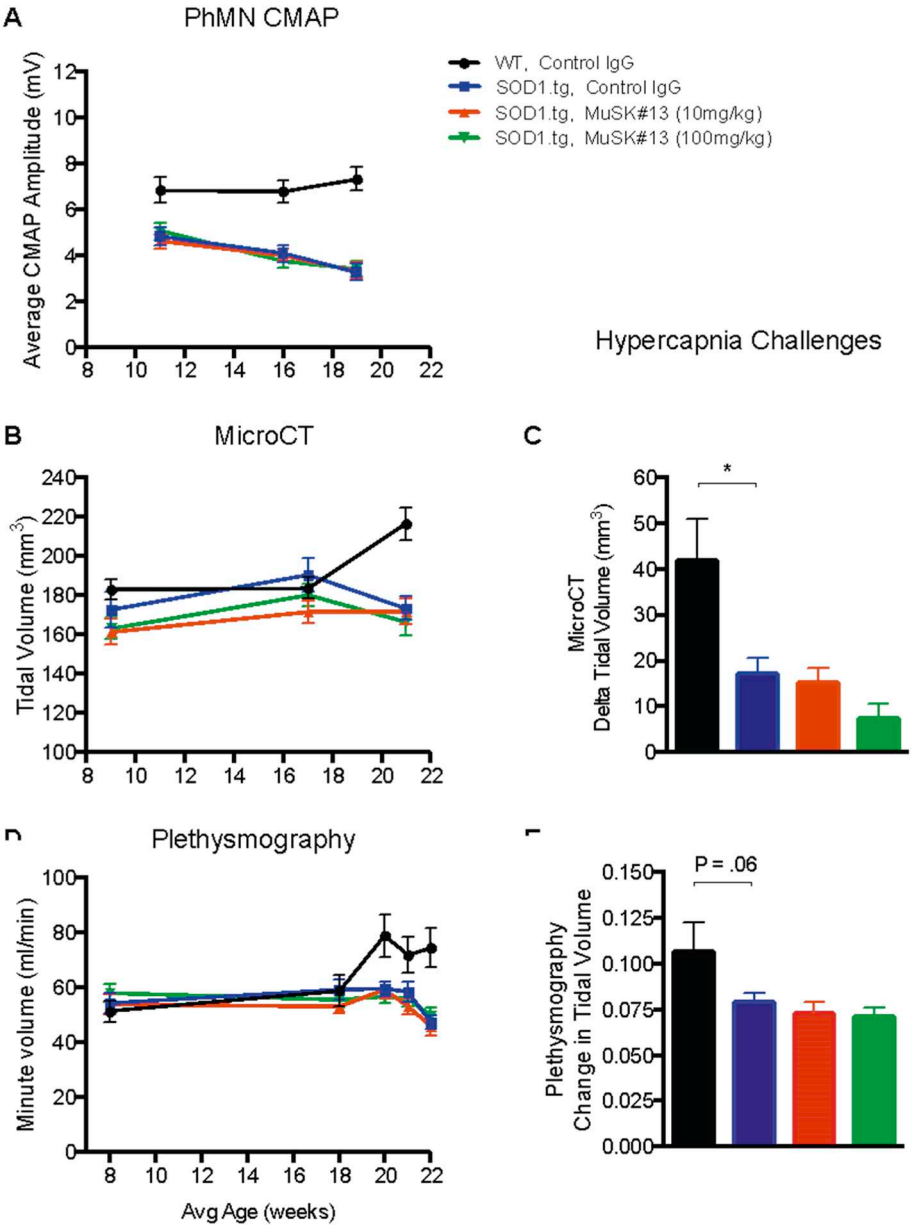

Fig. 4. Anti-MuSK does not alter diaphragm function. A. PhMN CMAP amplitude. RMANOVA (SOD1.tg, control IgG vs. WT, Control IgG) with factors genotype and time revealed significant effects of genotype ($F(1, 42) = 56.85$; $P < .0001$ but no time or interaction effect. When this same test was run across the 3 SOD1.tg treatment groups there was an effect of time ($F(2, 148) = 14.16$; $P < .0001$, but no effect of treatment and no interaction. This data suggests that CMAP amplitudes are altered by genotype and within the SOD1.tg groups across time but not by treatment. ($n = 18$ WT and 25–26 SOD1.tg/group). All data shown as ± SEM. B. Tidal Volume as measured by micro-CT. RMANOVA (SOD1.tg, control IgG vs. WT, Control IgG) with factors genotype and time revealed significant effects of genotype ($F(1, 36) = 11.71$; $P = .0016$, a time effect ($F(2, 72) = 11.54$; $P < .0001$ and a time/genotype interaction ($F(2, 72) = 8.586$; $P = .0005$. When this same test was run across the 3 SOD1.tg treatment groups there was an effect of time ($F(2, 128) = 39.08$; $P < .0001$, but no effect of treatment and no interaction. This data suggests that changes in tidal volumes are altered by genotype and across time but not by treatment in the SOD1.tg mice. ($n = 17$ WT and 21–24 SOD1.tg/group). Post hoc comparisons, *t*-test for each time point reveals a main effect of genotype at the 21 week time point only, suggesting that genotype related deficits in Tidal volume, via Micro CT are not significant until very close to end stage. All data shown as ± SEM. C. Delta Tidal Volume at 21 weeks with Hypercapnia Challenge. Unpaired *t*-test (SOD1.tg, control IgG vs. WT, Control IgG) reveals a significant effect of genotype$^{**}P = .0112$ ($n = 17$ WT, 20 SOD1.tg). Dunnett's multiple comparison test between the 3 SOD1.tg groups reveal no significant effect of treatment ($n = 20$–24 group). D. Minute Volume as measured by WBP. A 2-way ANOVA confirmed a significant genotype effect between SOD1.tg mice ($n = 22$–27) and their WT littermates (n = 18) on minute volume ($p = .00$). tidal volume ($p < .05$), and respiratory frequency ($p = .008$). Post-hoc analyses for each time point showed significant reductions in frequency at 20 ($p < .05$) and 22 weeks of age ($p < .01$ respectively) and at 20 ($p < .05$) and 22 weeks ($p < .001$) for minute volume. No effect of anti-MuSK treatment was detected E. Response to Hypercapnia Challenge in WBP. An unpaired *t*-test (SOD1.tg, control IgG vs. WT, Control IgG) revealed a nonsignificant effect of genotype $p = .06$ ($n = 17$ WT, 20 SOD1.tg) on change in tidal volume in response to elevated CO_2. One-way ANOVA across the 3 SOD1.tg groups reveal no significant effect of treatment (n = 20–24 SOD1.tg/group).

8.31% ± 1.85% in the 100 mg/kg dose (Fig. 3G-H). It was notable that 100 mg/kg MuSK #13 resulted in NMJ innervation that was comparable to wild-type mice. In addition, AchR expression level at the NMJs was measured by quantifying the number of pixels that were stained with alpha bungarotoxin per NMJ. No effect of genotype or treatment on AchR levels was detected (WT = 3969 ± 553, SOD1 = 4399 ± 297, SOD1 10 mg/kg = 4568 ± 457, SOD1 100 mg/kg = 4897 ± 490).

3.3. MuSK #13 does not benefit diaphragm or respiratory function in SOD1.Tg mice

To determine if the improvement in NMJ innervation leads to improved function of the diaphragm, we measured CMAP amplitude recorded from the diaphragm after stimulating the phrenic nerve at 11, 16, and 19 weeks of age in control- and MuSK-treated mice. MuSK #13 dosing began prior to any sign of CMAP amplitude reduction and was continued to 20 weeks of age, when reductions in CMAP amplitude are maximal (Fig. S2A). As expected, control-treated SOD1.tg mice had significantly reduced CMAP amplitudes compared to wild-type mice at 11 weeks (mean ± SEM: 4.8 ± 0.41 vs. 6.9 ± 0.58), 16 weeks (mean ± SEM: 4.1 ± 0.36 vs. 6.8 ± 0.49), and 19 weeks (mean ± SEM: 3.29 ± 0.38 vs. 7.3 ± 0.51) of age. Despite full NMJ innervation at 18 weeks of age with MuSK #13 treatment, no effect of MuSK #13 treatment was detected on CMAP amplitude of the diaphragm at any age (Fig. 4A). To determine whether preserved NMJ innervation of the diaphragm translated into improved respiratory function, micro-CT imaging of the lung was conducted at several time points throughout the study. Impairment of the diaphragm function leads to less air displacement during the inspiration, resulting in reduced tidal volume. Tidal volume, as evaluated by micro-CT imaging, is a direct measurement of the change in lung volume between peak inspiration and end-expiration. Mice were scanned on the micro-CT at 9, 17 and 21 weeks of age, and Tidal Volumes were estimated by automated image analysis. At 21 weeks of age, SOD1.tg mice had impaired lung function as detected by several imaging measures. Tidal Volume in

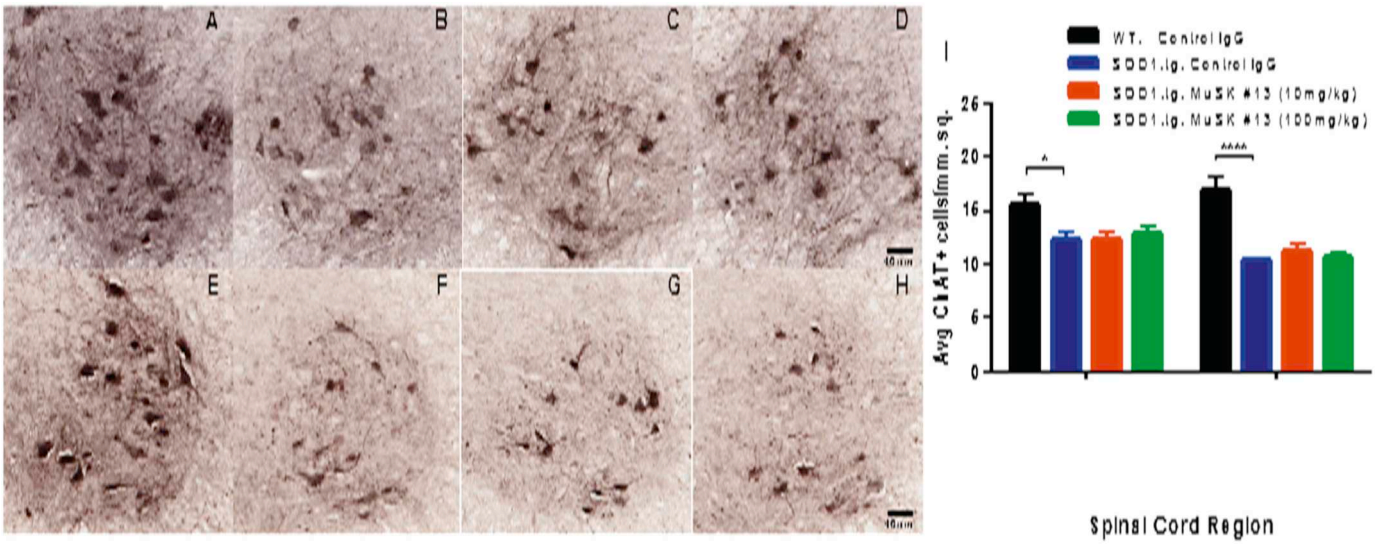

Fig. 5. Anti-MuSK treatment does not protect from Spinal Cord Motor Neuron Loss. A-D: Representative images of ChAT stained motor neurons in cervical spinal cord A. WT, Control IgG group B. SOD1.tg, Control IgG C. SOD1.tg, MuSK #13 (10 mg/kg) D. SOD1.tg, MuSK #13 (100 mg/kg) E. 2-Way ANOVA (SOD1.tg, control IgG vs. WT, Control IgG) with factors genotype and spinal cord region revealed significant effects of both genotype $F(1, 42) = 63.55$; $^{*}P < .0001$ and spinal cord region $F(2, 42) = 5.305$; $^{**}P = .0088$ as well as an interaction $F(2, 42) = 3.582$; $^{*}P = .0366$ with post hoc comparisons, t-test revealed a main effect of genotype for cervical ($^{*}P = .0152$) and lumbar ($^{****}P < .0001$) regions as well. 2-way ANOVA across the across the 3 SOD1.tg treatment groups there was an effect of spinal cord region $F(2, 72) = 7.179$; $P = .0014$ but no effect of treatment and no interaction ($n = 17$ WT and 21–24 SOD1.tg/group) followed by a post-hoc Dunnett's test which also showed no effect of treatment. An average of 12 spinal cord sections were quantified for each mouse. All data shown as ± SEM.

the control-treated SOD1.tg group was lower compared to wild-type mice (mean ± SEM: 176 ± 6 vs. 216 ± 9 mm^3, Fig. 4B). At earlier time points (9 and 17 weeks), no significant differences were observed. Under the hypercapnia condition at 21 weeks, the mean Tidal Volume was elevated from the air condition in all groups as the mice increased their ventilation in response to the challenge (Fig. 4C). The increase in Tidal Volume from air to hypercapnia (ie. the Delta Tidal Volume) was lower in the control-treated SOD1.tg group compared to WT mice (mean ± SEM: 17.2 ± 3.6 vs. 41.8 ± 9.1 mm^3), indicating that the SOD1.tg mice had a blunted response to the hypercapnia challenge. MuSK #13 treatment had no significant effect on Tidal Volume in SOD1.tg mice under air or hypercapnia condition, or on Delta Tidal Volume. A modest MuSK #13 treatment effect was observed in the end-expiratory lung volume. MuSK #13 groups, similarly to WT, had lower end-expiratory lung volume compared to the control IgG SOD1.tg group at weeks 17 and 21, but, this change in end-expiratory lung volume did not result in improvement of Tidal Volume (Fig. S3).

We also used whole body plethysmography to test whether the respiratory deficits seen in SOD1.tg mice could be altered with MuSK #13 treatment. Unlike the direct imaging of the lung, plethysmography measures inhaled and exhaled airflow in non-anesthetized mice. In this study, respiratory frequency, tidal volume, and minute volume were measured. SOD1.tg mice had reduced minute volume (59.56 +/− 2.63 ml/min) compared to WT mice (78.86 +/− 7.67 ml/min) by 20 weeks of age. Tidal volume and respiratory frequency were also significantly reduced at 22 eeks of age ($p < .01$). No effect of MuSK #13 treatment was detected on any of these measures when comparing the SOD1.tg groups ($n = 19–27$/group) (Fig. 4D). Furthermore, when these mice were challenged by adding 5% CO2 to the chamber, we observed a modest reduction of tidal volume response in SOD1.tg (0.08 ± 0.005 ml) compared to WT (0.1 ± 0.015 ml) but no effect of MuSK #13 treatment in the SOD1.tg mice (Fig. 4E).

3.4. MuSK #13 does not protect against motor neuron degeneration in the spinal cord and brainstem

Next, we determined whether preservation of NMJs in MuSK #13-treated mice might also lead to protection of the motor neuron cell body. Alpha-motoneurons were identified as ventral horn cells, which were positive for choline acetyl transferase (ChAT) immunoreactivity. ChAT-positive neurons were quantified in L3–5, the spinal cord region innervating the leg muscles, and in C3–5, the spinal cord region innervating the diaphragm at 18 weeks of age. While there was significant motor neuron loss in SOD1.tg mice in the C3–5 region, MuSK #13 treatment did not protect motor neurons from degeneration, despite the robust preservation of NMJs in the diaphragm (Figs. 5A-I & Fig. S1, panel B). This data suggests that preservation of neuromuscular synapses at the phrenic nerve terminal alone cannot protect against cervical motor neuron loss. As expected, we detected significant reduction of CHAT-positive neurons in the L3–5 region of SOD1.tg mice, but again found that dosing with MuSK #13 antibody did not protect against motor neuron degeneration.

In addition to motor neuron loss, we previously found that clear, variably sized vacuoles are present in the neuropil of the trigeminal, facial and hypoglossal nuclei, and fewer and smaller clear vacuoles were also seen in the ventral horns of the gray matter in the cervical spinal cord by 18 weeks of age (Supplemental Methods and Fig. S4). Transmission electron microscopy revealed these vacuoles were located within expanded axons. The vacuoles were intimately associated with abnormally shaped and markedly swollen mitochondria. The mitochondria were lined by disrupted outer membranes often forming extensive buds or protrusions filled with electron lucent vesicular structures and granular material expanding the intermembrane space, separating the outer membrane from the inner membranes (Supplemental Methods and Fig. S4). These histological findings likely explain imaging abnormalities detectable by MRI in the same regions of the brainstem and spinal cord of SOD1.tg mice (Xie et al., 2017).

To complement the motor neuron histology in this study, we used MRI to measure changes in T_2–weighted images in the brainstem and cervical spinal cord. Here we confirm the finding that T_2 values are higher in all SOD1.tg animals compared to the wildtype control IgG cohort, consistent with previously published T_2 MRI studies for the hindbrain (Zang et al., 2004; Niessen et al., 2006; Bucher et al., 2007) and spinal cord (Niessen et al., 2006). Lesions are visible in the

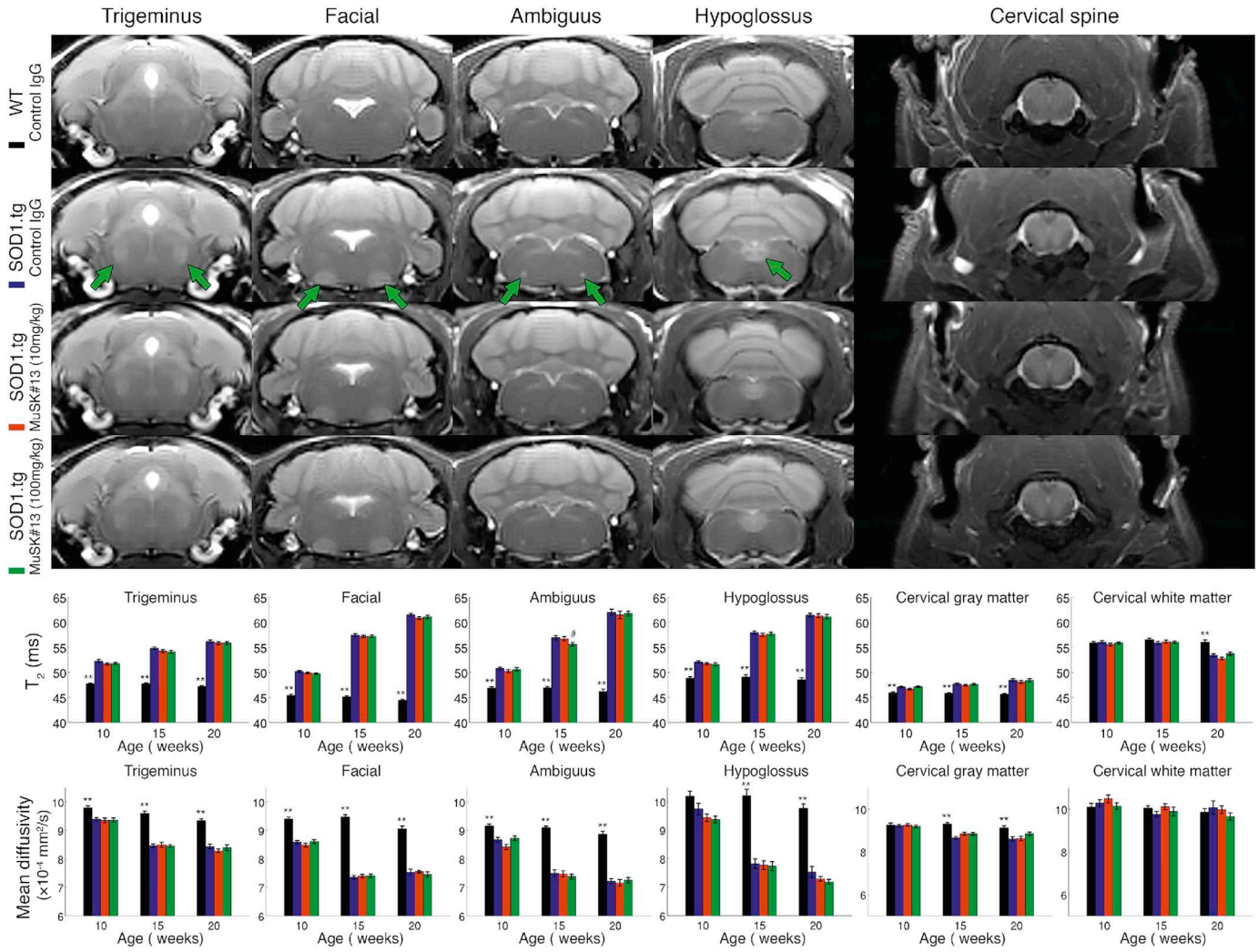

Fig. 6. Anti-MuSK treatment did not protect against brainstem or cord imaging abnormalities. Four cohorts were imaged in this study include 1) wildtype SOD1- Anti-gp120, 2) SOD1 + Anti-gp120, 3) SOD1 + Anti-Musk 10 mg/kg, and 4) SOD1 + Anti-Musk 100 mg/kg. *t*-tests were performed to determine differences between the cohorts. Tests were performed for all brain regions (hypoglossus, ambiguous, facial, trigeminus, cervical white matter, cervical gray matter) by all MRI metrics (T_2, FA, MD, AD, RD) at all time points (10, 15, 20 weeks). Significance was determined between cohorts and SOD1 + Anti-gp120. *P* values < .05 were considered statistically significant ($p < .05$ labeled with * and $p < .01$ labeled with **). t-test *p* values < .05 were considered statistically significant ($p < .05$ labeled with * and $p < .01$ labeled with **). Dunnett's test p values < .05 were considered statistically significant ($p < .05$ labeled with # and $p < .01$ labeled with ##). All plots are presented as means with standard error ($\mu \pm \sigma/\sqrt{n}$).

trigeminal nucleus, facial nucleus, nucleus ambiguus, and the hypoglossal nucleus of the hindbrain in SOD1.tg mice (Fig. 6). The T_2 difference between wildtype control and SOD1.tg increases with age from 10 weeks to 20 weeks. T_2 lesions were also detected at 20 weeks in the cervical white matter. MRI diffusion metrics have been demonstrated to both decrease and increase when comparing SOD1.tg animals with wildtype controls (Evans et al., 2014; Kim et al., 2011; Niessen et al., 2006; Towner et al., 2013), possibly due to differences in diffusion imaging methodology among these studies. Here we found that mean diffusivity values are reduced in the hindbrain lesions (Fig. 6), where genotype differences were detected at 10 weeks for trigeminus, facial, and ambiguus nuclei; and 15 weeks in the hypoglossus nucleus and cervical gray matter. A summary of statistical tests for MRI metrics of all brain regions is shown in S5 Table1. Similar to the motor neuron histology, no effect of MuSK #13 treatment (both 10 mg/kg and 100 mg/kg) was detected by MRI on brain or spinal cord T_2, or on diffusion abnormalities found in the SOD1.tg cohorts. Together, these histological and imaging results indicate that NMJ protection does not translate into protection of motor neuron cell bodies in the CNS.

3.5. MuSK #13 does not alter disease progression in SOD1.tg mice

To determine whether benefits in overall function could be observed with MuSK #13 treatment we examined disease symptom progression over the life span of the SOD1.tg mice by monitoring body weight loss and paralysis symptoms. Compared to WT, SOD1.tg mouse body weights declined beginning at around 17 weeks of age. As muscle atrophy is also occurring at the same time, we find that body weight is a reliable index of muscle mass and overall health of the animal. If treatment with MuSK #13 were preserving functional synapses across all muscle, one would expect that body weight changes would be rescued as well. Treatment with MuSK #13 did not increase body weight in SOD1.tg mice and did not delay the onset of weight loss (Fig. 7A). To understand disease progression more closely, development of paralysis was measured using the ALS-TDI scoring system. Starting at 112 days, mice were monitored for signs of paralysis using ALS TDI system scores 2–4 (Hatzipetros et al., 2015). If NMJs were to be protected in the leg similarly to the diaphragm, a delay in the progression of paralysis would be predicted (dosing of mice with the MuSK #13 antibody

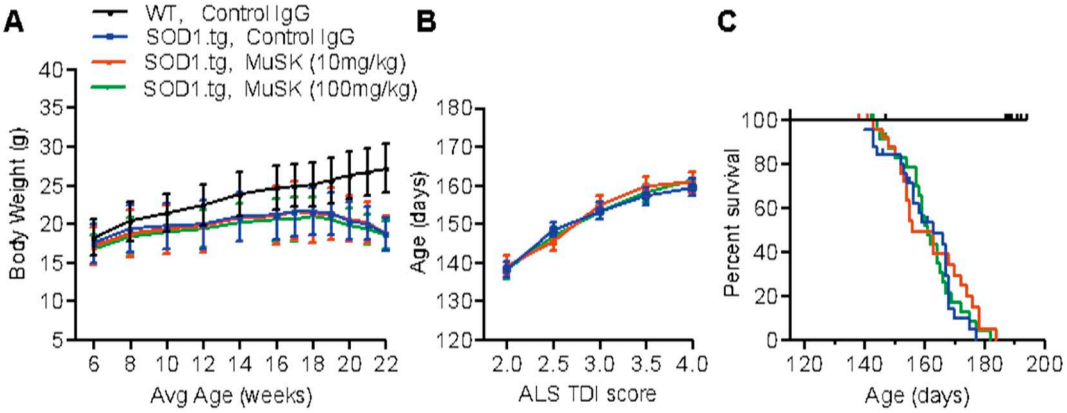

Fig. 7. Musk #13 treatment does not delay disease progression. A. Anti-MuSK treatment did not prevent body weight loss. RMANOVA was run for the 6–22 week time points, when the two Control IgG groups are compared with factors genotype and age, significant effects of genotype ($F(1, 36) = 17.10$; $P = .0002$ and age ($F(11, 396) = 169.6$; $P < .0001$ as well as a genotype/age interaction ($F(11, 396) = 169.6$; $P < .0001$ were observed. Next the 3 SOD1.tg groups were compared in a RMANOVA with the factors treatment and age which revealed an age effect ($F(11, 605) = 149.4$; $P < .0001$ but no treatment effect and no interaction. (n = 17 WT and 18–21 SOD1.tg /treatment) Post-hoc Dunnett's tests were performed comparing both SOD1.tg treatment groups to the SOD1.tg, Control IgG group at all remaining time points (23–26 weeks) where no significant treatment effect was observed. B. Anti-MuSK treatment did not alter the development of paralysis. Representative image displaying the average age that each group reached its ALS-TDI paralysis progression score. Since paws were monitored individually a score of 2.0 represents the age at which ALS TDI 2 was reached in one hind paw and a score of 2.5 represents the age at which ALS TDI 2 was observed in both paws and the same is true for scores of 3.0 and 3.5 (n = 17 WT and 21–27 SOD1.tg /treatment). Data shown as mean ± SEM. For statistical analysis see Table 1. C. Anti-MuSK treatment did not alter survival. Kaplan-Meier plot showing that the life spans of SOD1.tg mice are not altered by treatment (see Table 1) for p values and median life span (n = 17 WT and 22–23 SOD1.tg /treatment). Mice that were censored from this analysis, due to non-ALS related deaths, are represented by black dots, which are not accompanied by the lowering of the curve.

Table 1
ALS-TDI and survival analyses.

	Median time (days)			Median time (days)			Number failed			p value	
	Control IgG	Musk#13 (10 mg/kg)	MuSK#13 (100 mg/kg)	Control IgG	Musk#13 (10 mg/kg)	MuSK#13 (100 mg/kg)	Control IgG	Musk#13 (10 mg/kg)	MuSK#13 (100 mg/kg)	Log rank	Wilcoxon
ALS Score 2 (1 paw)	140	140.5	142	137.3	139.3	138.1	26	26	27	0.5676	0.9162
ALS Score 2 (both paws)	151	147	148	147.5	145.6	147	26	26	27	0.9366	0.5554
ALS Score 3 (1 paw)	156	151	155	153.5	155.1	153.3	23	25	26	0.6176	0.9716
ALS Score 3 (both paws)	158	155	159	157.3	159.9	158.1	22	23	21	0.6137	0.8887
ALS Score 4 (survival)	163	156	161	160.5	162	161.6	22	22	23	0.6897	0.9554

Kaplan-Meier survival fit tests were performed for each paralysis score. *P*-values were calculated using Log-rank and Wilcoxon calculations. No treatment effect was observed between SOD1.tg treatment groups for the onset of any of the five paralysis progression scores, including survival.

started before reported NMJ denervation in the leg muscle). In contrast, no delay was observed in the progression of paralysis symptoms in SOD1.tg mice treated with MuSK #13 (Fig. 7B and Table 1). Consistent with this finding, CMAP recordings performed in the lower leg muscle of the gastrocnemius from 4 to 16 weeks of age, in a separate cohort, were not altered (Fig. S6). Finally, no significant effect was detected for MuSK #13 treatment on survival in the SOD1.tg mice (Fig. 7C). Taken together, the data suggest that the preservation of neuromuscular synapses by MuSK activation does not functionally protect SOD1.tg mice and does not slow disease progression.

4. Discussion

Synapse loss at the neuromuscular junction is one of the major pathological events contributing to the decline of motor and respiratory function in patients with ALS. Here, we report similar degeneration in neuromuscular circuits regulating diaphragm function and respiration in SOD1.tg mice. We then tested whether MuSK activation might preserve synapses at the NMJ and prevent functional decline. Chronic treatment with a MuSK agonist antibody fully preserved the NMJs in the diaphragm in SOD1.tg mice. Despite achieving clear target engagement with the antibody, no benefit to diaphragm function or respiration was detected. Furthermore, motor neuron death and survival of the animal was not impacted. While lack of functional benefit raises concern regarding the benefit of MuSK antibody in ALS patients, additional studies could be performed to investigate potential benefit of this antibody in other diseases of the neuromuscular junction.

4.1. NMJ protection

Here we report that MuSK activating antibody, given in a prevention paradigm, was able to fully preserve innervation of the NMJ in the diaphragm of SOD1.tg mice. This finding is consistent with data from an independent study using the same antibody which also showed synapse protection, even after denervation of the NMJ has initiated (Cantor et al., 2018). NMJ protection has now been observed across several studies in which various means of achieving MuSK activation have been employed (Miyoshi et al., 2017; Perez-Garcia and Burden, 2012). In each of these studies, either limited functional benefit, or in this case, no functional benefit was detected.

The observation that anti-MuSK antibody preserved NMJ innervation without affecting motor neuron survival suggests that MuSK activation may have increased sprouting from remaining neurons or may be maintaining innervation of sprouted terminals. Axonal sprouting is a natural mechanism attempting to compensate muscle denervation in motoneuron diseases and after nerve trauma (Tam and Gordon, 2003), and is observed in ALS patient tissue (Frey et al., 2000). However, sprouting of collateral axons does not achieve sustained functional compensation in SOD1G93A mice (Mancuso et al., 2011). In mice, overexpression of the growth factor Neuregulin-1 induced robust sprouting but did result in significant improvement in motor function or survival in $SOD1^{G93A}$ mice (Mancuso et al., 2016). Lack of functional benefit with the MuSK antibody may therefore be due to impaired synaptic transmission in these sprouted axons (Tateno et al., 2009; Moller et al., 2017) or improper innervation of the muscle and lack of functional motor endplates.

The benefit of MuSK therapy is predicated on the finding that decay of the NMJ occurs early in the course of disease prior to motor neuron death and paralysis. This is a robust finding in the leg muscles of the SOD1.tg mouse which we and others have reported (Fischer et al., 2004; Le Pichon et al., 2017). This phenomenon was not as apparent at the level of the diaphragm where maximal NMJ loss occurred in a similar time frame to maximal motor neuron loss, between 15 and 18 weeks of age. Interestingly, one of the earliest detectable pathological findings was gray matter lesions in brainstem nuclei critical for respiratory regulation. Specifically, the nucleus ambiguus is a part of the ventral respiratory group that controls exhalation and, in concert with the dorsal respiratory group, determines the respiratory rate. Neurons projecting from the brainstem impinge on the phrenic nucleus in the cervical spinal cord, where significant T_2 lesions and decreased mean diffusivity were detected. Evans et al. attributed similar MRI findings (elevated T_2, reduced diffusion) to restricted tissue diffusion, inflammation, and glial activation, suggesting that changes in T_2 and mean diffusivity are not due to simple fluid accumulation, but reflect more complex events (Evans et al., 2014). Overall, our temporal characterization of pathology using imaging and histological techniques, indicate motor neuron degeneration starts in the brainstem and spinal cord as a result of the accumulation of vacuoles in the neuropil and mitochondrial abnormalities. This CNS pathology is accompanied by axonal degeneration and NMJ denervation of the diaphragm - key events ultimately leading to respiratory dysfunction (Llado et al., 2006; Bradley et al., 1983). Preserving the number of synaptic inputs to the diaphragm via MuSK activation may therefore be insufficient to compensate for the considerable motor neuron pathology already taking place.

4.2. Respiratory function

The earliest functional change detected in the respiratory circuit was a reduction in the diaphragm CMAP amplitude, which was partially reduced by 9 weeks of age. This initial reduction was concomitant with modest (~20%) denervation of the NMJ and prior to cervical motor neuron loss. Although not measured here, the initial reduction in CMAP amplitude could be attributed to reduced acetylcholine release from the phrenic nerve (Tateno et al., 2009). Axonal dysfunction such as the accumulation of neurofilaments and the slowing of axonal transport and synaptic vesicle release is reportedly an early pathological event in SOD1.tg mice (Williamson and Cleveland, 1999). Alternatively, the initial CMAP reduction could be attributed to dysfunction of muscle fibers related to intrinsic mutant SOD1 expression and mitochondrial dysfunction in this tissue (Leclerc et al., 2001; Dobrowolny et al., 2008). In future studies, it would be informative to examine the function and histopathology of both the phrenic nerve and muscle in more detail.

Reduction of CMAP amplitude between 15 and 20 weeks is likely driven by robust denervation of the NMJ at this time. Despite MuSK antibody preservation of synapse number, no functional improvement was detected in the diaphragm CMAP amplitude. Cantor et al. report preservation of the NMJs in the diaphragm congruent with functional benefit in an ex vivo CMAP assay (Cantor et al., 2018). We find these differences surprising given that we dosed higher and more frequently (100 mg/kg for 1 ×/14 days vs 1 ×/20 days), achieving 10-fold higher antibody concentrations in the plasma. However, differences in methods for measuring lung function may have resulted in differing outcomes. Cantor et al. assessed synaptic transmission at the NMJ by first removing the phrenic nerve and diaphragm from the animal and CMAP responses were measured upon repetitive stimulation of the phrenic nerve. It is conceivable that isolating the phrenic nerve and diaphragm from the CNS results in functional effects that cannot be obtained in the whole animal. The in vivo CMAP methods used here could reflect the action potentials from multiple thoracic muscles (Martin et al., 2015; Romer et al., 2017) and not purely the diaphragm. Though we did not measure NMJ innervation in neighboring muscle, we assume that MuSK antibody would provide similar protection in all muscles of thorax.

The SOD1.tg animal model is often referred to as an aggressive model, indicating that it may be difficult to rescue function in animals where neurodegeneration occurs quite early in adulthood. It is therefore worth noting that NMJ denervation of the diaphragm occurs much later than NMJ loss in the gastrocnemius. Differences between these two tissues may be in part due to differences in composition of fast twitch muscle vs slow twitch muscles. The diaphragm muscle is composed of ~50% slow twitch Type I, 20% FR fast twitch Type IIa, 30% FF Type IIb fast twitch. The largest caliber axons (Type II) are most susceptible to loss in SOD1.tg mice (Gordon et al., 2007) and in patients. Furthermore, loss of motor neurons in the lumbar cord was significantly greater than loss of motor neurons in the cervical cord. Despite the slower progression of degeneration of motor neurons innervating the diaphragm, MuSK antibody treatment was unable to affect function of this neuromuscular circuit. It might, however, be informative to test the MuSK antibody for functional effects in other mouse models of ALS, such as PFN1 mutant mice (Yang et al., 2016; Fil et al., 2017), where the primary cause of NMJ denervation differs from the SOD1 mouse.

MuSK activation is one of many muscle-directed strategies tested for efficacy in the SOD1 mouse model. Tirasemtiv, a small molecule activator of troponin, has been shown to improve diaphragm and EDL contractile force, respiration, and forelimb muscle strength in early stage mice but benefit was lost in later stages of the disease, and no survival benefit was detected (Hwee et al., 2014). Blockade of Nogo A, a neurite outgrowth inhibitor, increased innervation of the NMJ, muscle force and motor unit survival in early but not late stage disease in mice (Jokic et al., 2006; Bros-Facer et al., 2014). Furthermore, therapies aimed at troponin and Nogo A failed to meet primary endpoints in phase III and II clinical trials for ALS, respectively (Meininger et al., 2017; Collibee et al., 2018). Taken together, muscle-directed mechanisms appear to have limited benefit when given alone. However, such agents may provide benefit when given in combination with treatments targeting central motor neuron degeneration, such as inhibition of BAX (Gould et al., 2006) or the dual leucine zipper kinase (DLK, MAP3K12), an important regulator of the JNK pathway (Le Pichon et al., 2017).

4.3. Conclusion

MuSK activation fully and reproducibly prevents the loss of innervation of NMJs in the diaphragm in SOD1.tg mice. Lack of functional benefit in an ALS model is likely due to the multi-systemic nature of this disease in which structural, physiological, and metabolic impairments have been detected and multiple cell types are affected (for review see Casas et al., 2016). Nevertheless, the robust effect of MuSK antibody treatment on NMJ innervation warrants further investigation of its value as add-on therapy in ALS and for treatment of disorders of the neuromuscular junction such as Myasthenia Gravis or Lambert-Eaton Syndrome.

Acknowledgements

Many thanks to Kimberly Stark, Bill Meilandt, Colin Cox, Maria Martinez, Luz Orellana, Sheila Ulufatu, and Dongping He for their valuable contributions to these studies.

Disclosure statement

All authors are current or former employees of Genentech, Inc.

Appendix A. Supplementary data

Supplementary data to this article can be found online at https://doi.org/10.1016/j.nbd.2018.12.002.

References

Alexander, G.M., Erwin, K.L., Byers, N., Deitch, J.S., Augelli, B.J., Blankenhorn, E.P., Heiman-Patterson, T.D., 2004. Effect of transgene copy number on survival in the G93A SOD1 transgenic mouse model of ALS. Brain Res. Mol. Brain Res. 130, 7–15.

Barck, K.H., Bou-Reslan, H., Rastogi, U., Sakhuja, T., Long, J.E., Molina, R., Lima, A., Hamilton, P., Junttila, M.R., Johnson, L., Carano, R.A., 2015. Quantification of tumor burden in a genetically engineered mouse model of lung cancer by micro-CT and automated analysis. Transl. Oncol. 8 (2), 126–135.

Bradley, W.G., Good, P., Rasool, C.G., Adelman, L.S., 1983. Morphometric and biochemical studies of peripheral nerves in amyotrophic lateral sclerosis. Ann. Neurol. 14, 267–277.

Bros-Facer, V., Krull, D., Taylor, A., Dick, J.R., Bates, S.A., Cleveland, M.S., Prinjha, R.K., Greensmith, L., 2014. Treatment with an antibody directed against Nogo-A delays disease progression in the SOD1G93A mouse model of amyotrophic lateral sclerosis. Hum. Mol. Genet. 23 (16), 4187–4200 (Aug 15).

Bucher, S., Braunstein, K.E., Neissen, H.G., Kaulisch, T., Neumaier, M., Boeckers, T.M., Stiller, D., Ludolph, A.C., 2007. Eur. J. Neurosci. 26 (7), 1895–1901.

Burden, S.J., Yumoto, N., Zhang, W., 2013. The role of MuSK in synapse formation and neuromuscular disease. Cold Spring Harb. Perspect. Biol. 5, a009167.

Cantor, S., Zhang, W., Delestree, N., Remedio, L., Mentis, G.Z., Burdent, S.J., 2018. Preserving neuromuscular synapses in ALS by stimulating MuSK with a therapeutic agonist antibody. elife 7, e34375.

Casas, C., Manzanob, R., Vazc, R., Ostab, R., Britesc, D., 2016. Synaptic failure: focus in an integrative view of ALS. Brain Plasticity. 1 (2), 159–175.

Cole, R.N., Reddel, S.W., Gervasio, O.L., Phillips, W.D., 2008. Anti-MuSK patient antibodies disrupt the mouse neuromuscular junction. Ann. Neurol. 63 (6), 782–789.

Collibee, S.E., Bergnes, G., Muci, A., Browne 4th, W.F., Garard, M., Hinken, A.C., Russell, A.J., Suehiro, I., Hartman, J., Kawas, R., Lu, P.P., Lee, K.H., Marquez, D., Tomlinson, M., Xu, D., Kennedy, A., Hwee, D., Schaletzky, J., Leung, K., Malik, F.I., Morgans Jr, D.J., Morgan, B.P., 2018. Discovery of Tirasemtiv, the First Direct Fast Skeletal Muscle Troponin Activator. ACS Med. Chem. Lett. 9 (4), 354–358 (Feb 13).

Dechiara, T.M., Bown, D.C., Valenzuela, D.M., Simmons, M.V., Poueymirou, W.T., Thomas, S., Kinetz, E., Compton, D.L., Rojas, E., Park, J.S., Smith, C., Distefano, P.S., Glass, D.J., Burden, S.J., Yancopoulos, G.D., 1996. The receptor tyrosine kinase MuSK is required for neuromuscular junction formation in vivo. Cell 85 (4), 501–512.

Dobrowolny, G., Aucello, M., Rizzuto, E., Beccafico, S., Mammucari, C., Boncompagni, S., Belia, S., Wannenes, F., Nicoletti, C., Del Prete, Z., Rosenthal, N., Molinaro, M., Protasi, F., Fanò, G., Sandri, M., Musarò, A., 2008. Skeletal muscle is a primary target of SOD1G93A-mediated toxicity. Cell Metab. 8 (5), 425–436.

Engel, A.G., Shen, X.M., Selcen, D., Sine, S.M., 2015. Congenital Myasthenic Syndromes:pathogenesis, diagnosis, and treatment. Lancet Neurol. 14 (5), 461.

Evans, M.C., Serres, S., Khrapitchev, A.A., Stolp, H.B., Anthony, D.C., Talbot, K., Turner, M.R., Sibson, N.R., 2014. T_2-weighted MRI detects presymptomatic pathology in the SOD1 mouse model of ALS. J. Cereb. Blood Flow Metab. 34, 785–793.

Fil, D., DeLoach, A., Yadav, S., Alkam, D., MacNicol, M., Singh, A., Compadre, C.M., Goellner, J.J., O'Brien, C.A., Fahmi, T., Basnakian, A.G., Calingasan, N.Y., Klessner, J.L., Beal, F.M., Peters, O.M., Metterville, J., Brown Jr, R.H., Ling, K.K.Y., Rigo, F., Ozdinler, P.H., Kiaei, M., 2017. Mutant Profilin1 transgenic mice recapitulate cardinal features of motor neuron disease. Hum. Mol. Genet. 26 (4), 686–701 (Feb 15).

Fischer, L.R., Culver, D.G., Tennant, P., Davis, A.A., Wang, M., Castellano-Sanchez, A., Khan, J., Polak, M.A., Glass, J.D., 2004. Amyotrophic lateral sclerosis is a distal axonopathy: evidence in mice and man. Exp Neurol 185 (2), 232–240.

Frey, D., Schneider, C., Xu, L., Borg, J., Spooren, W., Caroni, P., 2000. Early and selective loss of neuromuscular Synapse subtypes with low sprouting competence in motor Neuron disease. J. Neurosci. 20 (7), 2534–2542.

Gordon, T., Putman, C.T., Hegedus, J., 2007. Amyotrophic lateral sclerosis - evidence of early denervation of fast-twitch muscles. Basic Applied Myology 17 (3&4), 141–145.

Gould, T.W., Buss, R.R., Vinsant, S., Prevette, D., Sun, W., Knudson, C.M., Milliegan, C.E., Oppenheim, R.W., 2006. J. Neurosci. 26 (34), 8774–8786.

Gurney, M.E., Pu, H., Chiu, A.Y., Dal Canto, M.C., Polchow, C.Y., et al., 1994. Motorneuron degeneration in mice that express a human Cu, Zn superoxide dismutase mutation. Science 264, 1772–1775.

Hatzipetros, T., Kidd, J.D., Moreno, A.J., Thompson, K., Gill, A., Vieira, F.G., 2015. A quick phenotypic neurological scoring system for evaluating disease progression in the SOD1-G93A mouse model of ALS. J. Vis. Exp.(104), e53257.

Herbst, R. and Burden, S.J. 2000. The juxtamembrane region of MuSK has a critical role in agrin-mediated signaling. EMBO J. 4;19(1):67–77.

Hwee, D.T., Kennedy, A., Ryans, J., Russell, A.J., Jia, Z., Hinken, A.C., Morgans, D.J., Malik, F.I., Jasper, J.R., 2014. Fast skeletal muscle troponin activator tirasemtiv increases muscle function and performance in the B6SJL-SOD1G93A ALS mouse model. PLoS One 9 (5), e96921 (May 7).

Jokic, N., Gonzalez de Aguilar, J.L., Dimou, L., Lin, S., Fergani, A., Ruegg, M.A., Schwab, M.E., Dupuis, L., Loeffler, J.P., 2006. The Neurite Outgrowth Inhibitor Nogo-A promotes denervation in an amyotrophic lateral sclerosis model. EMBO Rep. 7 (11), 1162–1167 (Nov).

Kim, J.H., et al., 2011. Noninvasive detection of brainstem and spinal cord axonal degeneration in an amyotrophic lateral sclerosis mouse model. NMR Biomed. 24, 163–169.

Kostic, V., Jackson-Lewis, V., de Bilbao, F., Dubois-Dauphin, M., Przedborski, S., 1997. Prolonging life in a transgenic mouse model of familial Amyotrophic Lateral Sclerosis. Science 277 (5325), 559–563.

Le Pichon, C., Dominguez, S.L., Solanoy, H., Ngu, H., Lewin-Koh, N., Chen, M., Eastham-Anderson, J., Watts, R., Scearce-Levie, K., 2013. EGFR inhibitor erlotinib delays disease progression but does not extend survival in the SOD1 mouse model of ALS. PLoS One 8, e62342.

Le Pichon, C.E., Meilandt, W.J., Dominguez, S., et al., 2017. Loss of dual leucine zipper kinase signaling is protective in animal models of neurodegenerative disease. Sci. Transl. Med. 16 (9), 403.

Leclerc, N., Ribera, F., Zoll, J., Warter, J.M., Poindron, P., Lampert, E., Borg, J., 2001. Selective changes in mitochondria respiratory properties in oxidative or glyocolytic muscle fibers isolated from G93AhumanSOD1 transgenic mice. Neuromuscul. Disord. 11 (8), 722–727.

Li, Z., Krippendorff, B.F., Sharma, S., Walz, A.C., Lavé, T., Shah, D.K., 2016. Influence of molecular size on tissue distribution of antibody fragments. In: MAbs. Vol. 8. Taylor & Francis, pp. 113–119 No. 1.

Livak, K.J., Schmittgen, T.D., 2001. Analysis of relative gene expression data using real-time quantitative PCR and the $2^{-\Delta\Delta Ct}$ method. Methods 25, 402–408.

Llado, J., Haenggeli, C., Pardo, A., Wong, V., Benson, L., Coccia, C., Rothstein, J.D., Shefner, J.M., Maragakis, N.J., 2006. Degeneration of respiratory motor neurons in the SOD1 G93A transgenic rat model of ALS. Neurobiol. Dis. 21 (1), 110–118.

Mancuso, R., Sasntos-Nogueira, Osta R., Navarro, X., 2011. Electrophysiological analysis of a murine model of motoneuron disease. Clin. Neurophysiol. 122 (8), 1660–1670.

Mancuso, R., Martinez-Muriana, A., Leiva, T., Gregorio, D., Ariza, L., Morrell, M., Esteban-Perez, J., Garcia-Redondo, A., Calvo, A.C., Atencia-Cibreiro, G., Corfas, G., Osta, R., Bosch, A., Navarro, X., 2016. Neurobiol. Dis. 95, 168–178.

Martin, M., Li, K., Wright, M.C., Lepore, A.C., 2015. Functional and morphological assessment of diaphragm innervation by phrenic motor neurons. J. Vis. Exp. (99), e52605 (May 25).

Meininger, V., Genge, A., van den Berg, L.H., Robberecht, W., Ludolph, A., Chio, A., Kim, S.H., Leigh, P.N., Kiernan, M.C., Shefner, J.M., Desnuelle, C., Morrison, K.E., Petri, S., Boswell, D., Temple, J., Mohindra, R., Davies, M., Bullman, J., Rees, P., Lavrov, A., NOG112264 Study Group, 2017. Safety and Efficacy of Ozanezumab in patients with amyotrophic lateral sclerosis: a randomized double-blind placebo-controlled phase 2 trial.

Miyoshi, S., Tezuka, T., Arimura, S., Tomono, T., Okada, T., Yamanashi, Y., 2017. DOK7 gene therapy enhances motor activity and life span in ALS model mice. EMBO Mol. Med. 9 (7), 880–889.

Moller, A., Bauer, C.S., Cohen, R.N., Webster, C.P., Devos, K.J., 2017. Amyotrophic lateral sclerosis-associated mutant SOD1 inhibits anterograde axonal transport of mitochondria by reducing Miro1 levels. Hum. Mol. Genet. 26 (23), 4668–4679.

Morsch, M., Reddel, S.W., Ghazanfari, N., Toyka, K.V., Phillips, W.D., 2012. Muscle specific kinase autoantibodies cause synaptic failure through progressive wastage of postsynaptic acetylcholine receptors. Exp. Neurol. 237 (2), 286–295.

Niessen, H.G., Engenstein, F., Sander, K., Kunz, W.S., Teuchert, M., Ludolph, A.C., Heinze, H.J., Scheich, H., Vielhaber, S., 2006. In vivo quantification of spinal and bulbar motor neuron degeneration in the G93A-SOD1 transgenic mouse model of ALS by T2 relaxation time and apparent diffusion coefficient. Exp. Neurol. 201, 293–300.

Perez-Garcia, M.J., Burden, S.J., 2012. Increasing MuSK activity delays denervation and improves motor function in ALS mice. Cell Rep. 2 (3), 497–502.

Romer, S.H., Seedle, K., Turner, S.M., Li, J., Baccei, M.L., Crone, S.A., 2017. Accessory respiratory muscles enhance ventilation in ALS model mice and are activated by excitatory V2a neurons. Exp. Neurol. 287 (Pt 2), 192–204.

Tam, S.L., Gordon, T., 2003. Mechanisms controlling axonal sprouting at the neuromuscular junction. J. Neurocytol. 32 (5–8), 961–974.

Tateno, M., Kato, S., Sakurai, T., Nukina, N., Takahashi, R., 2009. Mutant SOD1 impairs axonal transport of choline acetyltransferase and acetylcholine release by sequestering KAP3. Hum. Mol. Genet. 18, 942–955.

Towner, R.A., et al., 2013. In vivo detection of free radicals using molecular MRI and immuno-spin trapping in a mouse model for amyotrophic lateral sclerosis. Free Radic. Biol. Med. 63, 351–360.

Van de Lest, C.H., Versteeg, E.M., Veerkamp, J.H., Van Kuppevelt, T.H., 1995. Elimination of autofluorescence in immunofluorescence microscopy with digital image processing. J. Histochem. Cytochem. 43 (7), 727–730.

Veta, M., van Diest, P.J., Kornegoor, R., Huisman, A., Viergever, M.A., Pluim, J.P., 2013 Jul 29. Automatic nuclei segmentation in H&E stained breast cancer histopathology images. PLoS One 8 (7), e70221.

Williamson, T.L., Cleveland, D.W., 1999. Slowing of axonal transport is a very early event in the toxicity of ALS-linked SOD1 mutants to motor neurons. Nat. Neurosci. 2 (1), 50–56.

Xie, M.H., Yuan, J., Adams, C., Gurney, A., 1997. Direct demonstration of MuSK

involvement in acetylcholine receptor clustering through identification of agonist ScFv. Nat. Biotechnol. 15 (8), 768–771.
Xie, L., Brendza, R., Hedehus, M., Dominguez, S., Foreman, O., Ghosh, A., Meilandt, W., Ayalon, G., Carano, R., 2017. Diffusion and T2 Characterizations in Hindbrain and Spinal Cord in SOD1 Mouse Model of ALS. In: ISMRM 25th Annual Meeting and Exhibition, Honolulu, Hawaii, USA, pp. 0617.
Yang, C., Danielson, E.W., Qiao, T., Metterville, J., Brown Jr, R.H., Landers, J.E., Xu, Z., 2016. Mutant PFN1 causes ALS phenotypes and progressive motor neuron degeneration in mice by a gain of toxicity. Proc. Natl. Acad. Sci. U. S. A. 113 (41), E6209–E6218 (Oct 11).
Yip, V., Palma, E., Tesar, D.B., Mundo, E.E., Bumbaca, D., Torres, E.K., Reyes, N.A., Shen, B.Q., Fielder, P.J., Prabhu, S., Khawli, L.A., 2014. Quantitative cumulative biodistribution of antibodies in mice: Effect of modulating binding affinity to the neonatal Fc receptor. In: MAbs. Vol. 6. Taylor & Francis, pp. 689–696 May 1. No. 3.
Yumoto, N., Kim, N., Burden, S.J., 2012. Lrp4 is a retrograde signal for presynaptic differentiation at neuromuscular synapses. Nature 489, 438–442.
Zang, D.W., Yang, Q., Wang, H.X., Egan, G., Lopes, E.C., Cheema, S.S., 2004. Magnetic Resonance Imaging Reveals Neuronal Degeneration in the Brainstem of the Superoxide Dismutase 1 Transgenic Mouse Model of Amyotrophic Lateral Sclerosis. Eur. J. Neurosci. 20 (7), 1745–1751.